

# UNIVERSITY OF TWENTE.

Faculty of Engineering Technology

## Influence of Bovine Spermataozoa Bundling on Flagellar Wave Propagation

Yohan J.P. Le Gars

Bachelor's Thesis

BE-819

August 2021

---

**Chairman:**

prof. dr. S. Misra

**Supervisor:**

dr. I.S.M. Khalil

Surgical Robotics Laboratory  
Department of Biomechanical Engineering  
Faculty of Engineering technology  
University of Twente  
7522 AE Enschede  
The Netherlands

---

# Influence of Bovine Spermatozoa Bundling on Flagellar Wave Propagation

Yohan.J.P. Le Gars\*

*University of Twente, Faculty of Engineering Technology, Department of Biomechanical Engineering, Surgical Robotics Laboratory, 7522 AE, Enschede, The Netherlands*

*\*y.j.p.legars@student.utwente.nl*

**ABSTRACT:** Spermatozoa assemble into bundles to increase their net propulsive thrust and swimming speed in viscous fluids. Here, we study the time-dependent short-range hydrodynamic interactions of Bovine sperm cells on converging courses during bundle formation. The time-dependent wave variables of actively propagating waves along the flagella are measured to reveal the influence of bundling on the waveform during flagellar propulsion. Our theoretical predictions and experimental results show how the waveform vary during three bundling phases, consisting of far field-to-locking, spin-rolling, and steady-swimming. We show that sperm cells adapt to their surroundings by synchronizing their mean flagellar curvature, amplitude rise, and wavelength of their actively propagating waves, and assemble into bundles to increase their swimming speed.

**Key words:** sperm cell, flagellar beat pattern, sperm bundling, wave-variables

## 1 INTRODUCTION

Microorganisms often display efficient locomotion strategies and properties in their environment. These locomotion strategies have inspired engineers to mimic biology, also referred as biomimetics, to design tetherless micro-devices for microscale applications [1]. In nature, cells have evolved an astonishing array of appendages, structures, and kinematic strategies to generate superior propulsive thrust in viscous fluids [2]. Their propulsion mechanisms depend on the properties of the flow which are defined by the Reynolds number ( $Re$ ) that quantifies the relative magnitudes of viscous and inertial forces acting upon by the surrounding fluid. In the microscopic world where viscous forces are dominant, the swimming conditions are characterized by low Reynolds numbers ( $Re \ll 1$ ), resulting in negligible inertial forces. The implication is that a motion can be canceled completely during a complete time-periodic motion. Microorganisms have overcome this constraint by changing their shape in a nonreciprocal periodic way, by means of rotating one or several flagella in a helical and planar fashion, thereby breaking time reversal symmetry [3, 4]. Replicating the efficient flagellar propulsion of living cells in low Reynolds numbers regimes has become one of the main targets of micro- and nanorobotics for medical practices.

### 1.1 Framework

In recent decades, the propulsion mechanism of mammalian sperm cells have been mimicked for the development of tetherless soft micro robot [5, 6]. Among the microorganisms living in our bodies, sperm cells are considered to be fast paced [7]. They owe their speed in viscous medium to their flagella that initiate transverse bending waves propelling them forward [8]. On their way to the fertilization site, spermatozoa swim against various physiological medium by swimming along circular paths near surfaces and along helical paths far from any boundary surfaces due to their observed asymmetric flagellar bending waves [9]. As a result, these non zero curvature trajectories cover a wider surface area making it easier to find the egg. Furthermore, when a viscosity change occurs in the background fluid spermatozoa transition between planar and helical flagellar propulsion allowing them to maintain a relatively high speed regardless of the rheological and physical properties of the medium [5]. These undulatory systems are therefore attractive for achieving controlled actuation by means of an external stimulus. Due to their small size, sperm microrobots could reduce the level of intervention and help clinicians to access small spaces within the human body in a noninvasive manner which has the potential to decrease complications from traditional surgery procedures [10].

The improved computational power enable modern studies to perform high precision tracking of sperm cells in order to investigate the flagellar wave of the cells [9, 6]. The wave variables can be reconstructed from the analysis of high-speed videography where the cells are hydrodynamically trapped near a surface allowing to confine the flagellar beating in a planar fashion, facilitating sperm tracking [11]. Instantaneous velocities of the sperms' head were determined using resistive force theory and were shown to oscillate with the frequency  $\omega$  of the flagellar beat. Subsequently, the observed curved swimming paths are a consequence of chiral propulsion by asymmetric flagellar bending waves which are dependent on the viscosity of the fluid [9]. Additionally, the velocity field given the force exerted by the flagellum on the surrounding fluid can be determined using stokeslets flow field theory. Khalil et al. demonstrated that the velocity field created in close proximity to the beating tail is greater than near the head at relatively low actuation frequencies. As a consequence, the pressure gradient in close proximity to the distal tip of the flagellum is higher than the pressure close to the head, and results in propulsion enhancement [5]. Flow fields, propulsive thrust and frequency responses for motile sperm cells with a single flagellum have been determined, allowing the realization of soft actuated microrobots for in vitro experiments. The key requirements for in vivo applications are biocompatibility with soft human tissues, remote control mechanisms, highly efficient locomotion in the low Reynolds number regime under physiological conditions and cargo pick-up/drop-off mechanisms [12].

Several prototypes have been created and were successfully controlled via external magnetic fields. Magdanz et al. were the pioneer group to use real sperm cells to propel a microrobot by encapsulating them inside magnetic microtubes that can be remotely controlled with low external magnetic fields [13]. Recently, Khalil et al have realized several magnetic sperm-templated microrobots by assembling nanoparticles on bovine sperm cells. These sperm-templated microrobot can swim with asymmetrical and symmetrical flow field by changing the location of the magnetized particles on the flagellum. Since they are fabricated from a sperm template, they are highly compliant, biodegradable, and biocompatible. Al-

though actuated at frequencies comparable to that of live cells, their maximum swimming speed is still six times lower than ATP-driven cells [6]. As of today, generating high propulsive thrust with a relatively weak magnetic field against nonuniform flowing streams of bodily fluids remains a challenge that inhibits the transition towards in vivo applications [14].

It has been observed that sperm cells can increase their propulsive thrust in order to overcome the drag force on their head by bundling with other sperm cells, resulting in multiple flagella. Many guidance mechanisms help spermatozoa reach the fertilization site. Besides chemotaxis (behaviour of sperm cells in response to chemicals), fluid flows, temperature gradients and surfaces, interactions between several sperm also play a role [15]. Especially in murine or rodent sperm with a flat sperm head, bundling is favoured [16, 17]. Known as sperm trains, these spermatozoa attach by their heads which results in collective swimming with increased velocity. Empirical data have shown that sperm trains achieve greater velocity, not by increasing speed but by travelling in a more direct path than solitary cell [18]. Further, viscoelasticity of the medium was found to promote collective behavior of sperm [19]. Hence, cell-cell interactions seem to play a promoting role in successful sperm migration to the fertilization site, but few studies have investigated this phenomenon in mammalian sperm [20]. Multiflagellated sperm and tight bundling of long sperm (in the millimeter range) is found in many insects and remains an interesting phenomenon to be studied [21, 22].

## 1.2 Aims and Approach

This article focus on the influence of sperm bundling on the flagellar waveform of sperm cells in two different viscosities medium. These two different scenarios are presented in section A of Appendix. The flagellar waveform is analysed when the sperm cells assemble into bundles, which involves far field, spinning, and steady swimming phases. These transition and steady state phases are investigated by measuring time-dependent wave variables to characterize the flagellar propulsion using Fourier decomposition of the waveform. Since dynamical systems in nature

often line-up their motion for greater effectivity, the following research questions for a sperm clustering behavior arise:

- Do flagella when they do not yet interact have a different beat?
- When they interact do these beats synchronize or do they further disperse? The former is expected.
- How does the bundling influence the flagellar beat?

The mathematical approach in Friedrich serves as a guideline to perform the analysis.

First, a high precision tracking data of the flagellum changing shape from high speed video microscopy is carried out to extract the shape of the flagellar beat. The reconstruction of the flagellar wave form allows to observe the evolution of the flagella waves during the transition from single sperm cells to a bundle. The interactions between the beating flagella are studied to discover the optimal flagellar beat pattern of each flagellum to enhance the propulsion of the bundle. Furthermore, the speed difference of a single sperm cell and sperm bundle can also be determined.

The remainder of the report is organized as follows. In Section 2, the theory of flagellar propulsion is explained. Section 3 presents the high precision tracking method that is used and the results that ensue. Section 4 covers the discussion of these results. Finally, the conclusion and recommendations for future work are given in Section 6.

## 2 PRINCIPLES OF FLAGELLAR PROPULSION FROM SINGLE TO BUNDLE

The questions that arose in the introduction can be answered by reconstructing a model that is dependent on experimental data. This model omits parts of the dynamics that are taking place but the overall picture is still present. In this section, we shall go over the mathematical model used for a single sperm cell and see that it can be utilized for analysing spermatozoa bundling.

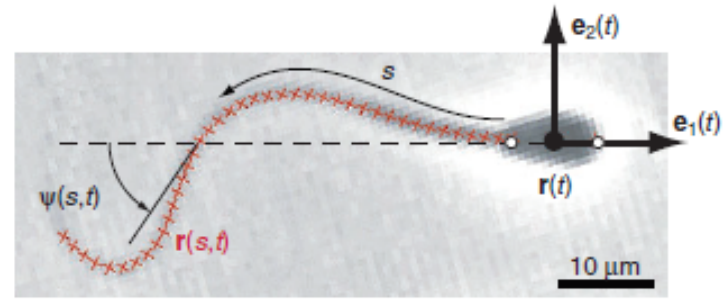


Fig. 1: Snapshot of a beating bull sperm at time  $t$ . Orthonormal vectors  $\mathbf{e}_1$  and  $\mathbf{e}_2$  are material frame for the sperm head. The shape of the flagellum is characterized by the tangent angle  $\psi(s, t)$  as a function of arc length  $s$  [9].

### 2.1 Kinematics of Single sperm Cells

Spermatozoa show a distinct mechanism of propulsion. This propulsion mechanism relies on the propagation of transverse bending waves along the flagella. Let us assume that the flagellum is a passive elastic filament close to a planar boundary surface inside a viscous fluid. The analysis can therefore be simplified to a two-dimensional projection where any out of plane component of the flagellar beat are neglected.

Fig.1 shows a snapshot of a beating bull sperm with a material frame for the sperm head denoted by a vector  $\mathbf{e}_1$  parallel to the long axis of the head and  $\mathbf{e}_2$  orthonormal to  $\mathbf{e}_1$ . Let express  $\mathbf{r}(s, t)$  as the position vector that denotes each points at a given time  $t$  along the arc length of the centerline,  $s$ . Subsequently,  $\mathbf{r}(s, t)$  is expressed with respect to the material frame of the sperm head whith  $\mathbf{r}(t)$  being the position of the head,  $\mathbf{r} + r_1\mathbf{e}_1$  and  $\mathbf{r} - r_1\mathbf{e}_1$  corresponding to the proximal tip and proximal end respectively. The shape of the flagellar centerline  $\mathbf{r}(s, t)$  can be characterized by a tangent angle  $\psi(s, t)$  that is measured for each arc length position and denotes the angle enclosed by the vector  $\mathbf{e}_1(t)$  and the tangent vector to the flagellar centreline at  $\mathbf{r}(s, t)$  (Fig.1). As stated in Friedrich work, the full flagellar beat pattern can be reconstructed with the above variables:

$$\begin{aligned} \mathbf{r}(s, t) = & \mathbf{r}(t) - r_1\mathbf{e}_1(t) \\ & - \int_0^s \cos \psi(u, t)\mathbf{e}_1(t) + \sin \psi(u, t)\mathbf{e}_2(t), \end{aligned} \quad (1)$$

and the beat pattern can be simplified by taking the following tangent angle:

$$\psi(s, t) = K_0 s + 2A_0 s \cos(\omega t - 2\pi s/\lambda) \quad (2)$$

where the wave variables  $K_0$  and  $A_0$  are the curvature and bending amplitude of the wave pattern and  $\lambda$  is the wavelength. For positive  $K_0 > 0$ , the flagellar beat bends more toward the positive direction of the axis  $\mathbf{e}_2(t)$ , while for negative mean flagellar curvature  $K_0 < 0$  the flagellar beat bends more toward the negative  $\mathbf{e}_1(t)$ . As a consequence, spermatozoa display an asymmetric flagellar beat as mentioned in the introduction.

Now let us consider a reference frame  $xy$  denoting the plane of swimming. The cartesian coordinates  $(x, y)$  and angular displacement  $(\theta)$  can be measured with respect to the reference frame and related to the cell body frame  $(\mathbf{e}_1(t), \mathbf{e}_2(t))$ . These cartesian coordinates can be written as [23] :

$$\begin{aligned} x(s, t) &= x_0 + \int_0^s \cos\psi(u, t) du, \\ y(s, t) &= y_0 + \int_0^s \sin\psi(u, t) du, \end{aligned} \quad (3)$$

and provide kinematic description of the flagellar shape. Further derivations such as the hydrodynamic drag force density  $\mathbf{f}(s)$  acting on cylindrical portion of the filament can be mathematically written:

$$\mathbf{f}(s, t) = \xi_{\perp} v_{\perp}(s, t) + \xi_{\parallel} v_{\parallel}(s, t), \quad (4)$$

where  $v_{\perp}(s, t)$  and  $v_{\parallel}(s, t)$  are the velocity components parallel and perpendicular to the filament centerline respectively. For more detailed derivations, see Friedrich [9].

Integrating the force from Eq.4 over the length gives the net thrust force :

$$\mathbf{f}_{visc} = \int_0^L ds \mathbf{f}(s, t) \quad (5)$$

Subsequently, the translational velocities can be retrieved based on the thrust force of the flagellum which in turn depends on the measurements of points along the arc length of the centreline provided by Eq.3:

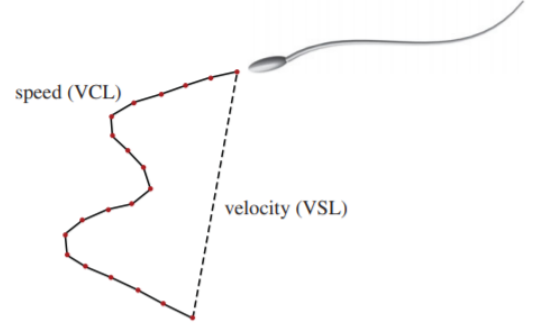


Fig. 2: Schematic of the average velocity (VSL) and speed (VCL). VSL is calculated by dividing the distance between the initial and final position in a sperm trajectory (dashed line) by the time  $\Delta t$  employed to move; VCL is found by dividing the length of the actual curvilinear trajectory (solid line) by  $\Delta t$  [18].

$$\begin{aligned} V_x &= \frac{1}{6\pi\eta a C_1} f_{visc}^x \\ V_y &= \frac{1}{6\pi\eta a C_2} f_{visc}^y \end{aligned} \quad (6)$$

The waves variables from Eq.2 are therefore key variables that completely characterize the flagellar beat of the sperm cell. Using RFT, the swimming velocities can be calculated as displayed above. Additionally, velocity and pressure field can be determined using RST.

Lastly, experimental velocities can be characterized into two categories. The average linear velocity or straightline velocity VSL and the swimming speed or curvilinear velocity VCL as shown in Fig.2.

The linearity of the trajectory is found by the expression  $VSL/VCL$  and describes the straightness of the swimming path taken by the sperm cells.

## 2.2 Characterization of spermatozoa bundling

The swimming phenomena of a bundle consists of the following phases: (1) far-field-to-locking phase; (2) spin-rolling transition phase; and (3) steady swimming phase. In the far-field-to-locking phase, the cells, being single, are influenced by far field flow created by neighbor swimming cells before assembling into bundle. Once they are locked, the cells undergo a spin-rolling motion about the vertical axis to reach a

stable configuration. This stable configuration is characterized by the alignment of the long axis of both heads' cells. If this stable configuration is reached, the sperm bundle swims by a regular flagellar beat.

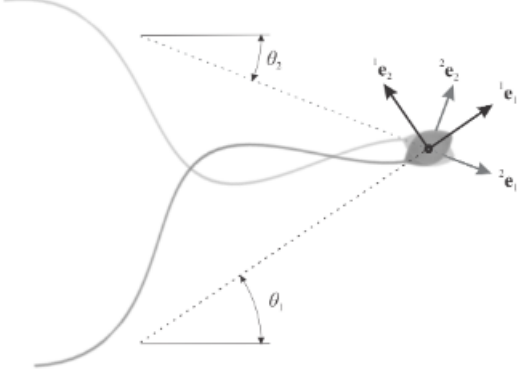


Fig. 3: 2 sperm cells are superimposed onto each other after a bundle.  ${}^i\mathbf{e}_1$  and  ${}^i\mathbf{e}_2$  are orthonormal unit vector of the  $i$ th cell such that  ${}^i\mathbf{e}_1$  is oriented along the long axis of the head.

Eq.1 can be re-written for the bundling problem as follows:

$${}^i\mathbf{r}(s, t) = {}^i\mathbf{r}(t) - r_1 {}^i\mathbf{e}_1(t) - \int_0^s \cos {}^i\psi(v, t) {}^i\mathbf{e}_1(t) + \sin {}^i\psi(v, t) {}^i\mathbf{e}_2(t) dv, \quad (7)$$

where  $i$  denotes the  $i$ th cell, illustrated in Fig.3. From there, all equations displayed above can be re-written in this fashion and tangent angles, velocities, thrust forces for each cells can be determined for every beat cycles at each swimming phase. The influence of each swimming phase on the flagellar beating can therefore be analyzed for two videos with viscosities of 1.2 and 7 mPas.

### 3 TIME-DEPENDENT WAVE VARIABLES

#### 3.1 Fourier Analysis of The Wave Pattern

The motion of bovine sperm cells is observed in fluids with viscosities of 1.2 and 7 mPa s and the flagellar waveform is measured while forming bundles. By splitting up both videos into frames, a fourier analysis is performed to determine the full flagellar beat

throughout the three swimming phases. The kinematic equations (3) are used to fit a smooth function in time and space to experimental data. These experimental data are taken from points coordinates located along the centerline of the flagellum and the tangent angle for each point along the arc length are then measured from consecutive beat cycles of the flagellum. The tangent angle of the flagellum can be decomposed of its zeroth and first Fourier mode as higher modes contribute less than 5% to the power spectrum :

$${}^i\psi(s, t) \approx {}^i\psi_0(s) + {}^i\psi_1(s)e^{i\omega t} + {}^i\psi_1^*(s)e^{-i\omega t}, \quad (8)$$

where  ${}^i\psi_0(s)$  is the zeroth mode characterizing the time averaged mean shape of the  $i$ th flagellum . The first mode  ${}^i\psi_1^*$  denotes the complex conjugate of  ${}^i\psi_1$ . From the Fourier decomposition (Eq.8), the following three waves variables that characterize the wave pattern are obtained:

$$\begin{aligned} {}^iK_0s &= {}^i\psi_0(s), \\ {}^iA_0s &= |{}^i\psi_1(s)|, \\ 2\pi s/\lambda &= -arg {}^i\psi_1(s), \end{aligned} \quad (9)$$

By fitting a line to the zeroth mode, the slope gives the mean flagellar curvature  $K_0$ . Similarly, the slope of the fitting line to the absolute value of the first mode  $|\psi_1(s)|$  gives the amplitude parameter  $A_0$ . Finally,  $\lambda$  is defined by taking the inverse of the fitting line multiplied by  $2\pi$ . The procedure is shown in Fig.10 (see Appendix).

As already stated in the previous section, the parameter  $K_0$  measures the asymmetry of the mean shape of the flagellum, the amplitude  $A_0$  indicates the bending amplitude along the arc length and  $\lambda$  is the wavelength, which indicates the speed of wave propagation along the flagellum. These time-dependent waves variables for both videos can then be determined and plotted versus time. Furthermore, the mean of the wave variables for each swimming phase can be put inside Eq.2 so that velocities, thrust forces and flagellar wave form can be retrieved.

#### 3.2 Transition in High Viscosity Medium

In experiments with relatively high viscosity of  $\mu = 7$  mPa, two cells assemble into bundles, as shown in Fig.13. In this case, the flagellar waveform of the three bundling phases are measured to determine the influence of each phase on the time-dependent

wave variables of both cells. In this experiment, the two cells collide on an orthogonal converging course (Fig.13 a-b). In the far field-to-locking phase, the averaged mean flagellar curvature of the first and second cells are  $\langle {}^1K_0 \rangle = 7.3 \pm 0.8$  and  $\langle {}^2K_0 \rangle = 8.9 \pm 1.09$  rad mm<sup>-1</sup>, respectively. As the distance between the cells decreases, the mean flagellar curvature of the first and second cells increases linearly. During the same phase, the flagellar amplitude of the first and second cells increases and decreases linearly as the distance between them decreases, and their average amplitude rise are  $\langle {}^1A_0 \rangle = 12.5 \pm 0.7$  and  $\langle {}^2A_0 \rangle = 9.4 \pm 0.8$  rad mm<sup>-1</sup>, respectively, as shown in Fig.4. Finally, the wavelength of the first cell during this phase decreases linearly with the distance between the cells and its average is  $\langle \lambda_1 \rangle = 40.1 \pm 2.6 \mu\text{m}$ , while the average wave length of the second cell remained almost uniform with an average of  $\langle \lambda_2 \rangle = 36.01 \pm 0.8 \mu\text{m}$ .

Once the heads of the two cells touch, they start the spin-rolling phase in which the two cells rotate about the common axis  ${}^i\mathbf{e}_1 \times {}^i\mathbf{e}_2$ . Note that the connection between the phases is continuous and the mean flagellar curvature of the first cell knows multiple increases and decreases, while that of the second cell slightly decreases in the first half of the spin-rolling phase and exhibits a slight increase in the second half. The average mean flagellar curvatures of the first and second cells during the spin-rolling phase are  $\langle {}^1K_0 \rangle = 8.02 \pm 2.2$  and  $\langle {}^2K_0 \rangle = 8.8 \pm 1.8$  rad mm<sup>-1</sup>, respectively. Unlike the mean flagellar curvature, there is a noticeable decrease at a constant rate in the amplitude rise throughout the spin-rolling phase for both cells. The average amplitude rise of the first and second cell during this phase are  $\langle {}^1A_0 \rangle = 10.6 \pm 1.6$  and  $\langle {}^2A_0 \rangle = 8.3 \pm 1.7$  rad mm<sup>-1</sup>. Finally, the wavelengths

exhibit multiple increases and decreases during the spin-rolling phase and the average are calculated as  $\langle \lambda_1 \rangle = 40.06 \pm 3.8 \mu\text{m}$  and  $\langle \lambda_2 \rangle = 39.7 \pm 5.4 \mu\text{m}$ , respectively. Note that there is a noticeable match between the three variables near the end of the spin-rolling phase near the 5 s mark.

Again once the long axes of the two heads align, the bundle starts the steady-swimming phase and we observe that the respective mean flagellar curvatures and bending amplitudes of the cells closely match. In this phase, the mean flagellar curvature of the first and second cells are  $\langle {}^1K_0 \rangle = 7.9 \pm 1.1$  and  $\langle {}^2K_0 \rangle = 8.2 \pm 0.9$  rad mm<sup>-1</sup>, respectively, while their corresponding bending amplitude are  $\langle {}^1A_0 \rangle = 7.5 \pm 1.3$  and  $\langle {}^2A_0 \rangle = 6.1 \pm 1.5$  rad mm<sup>-1</sup>, and no noticeable change throughout this phase is observed. Unlike the mean flagellar curvature and amplitude rise, there is a noticeable difference in the wavelength before and after the steady-swimming phase, and the first and second cells have  $\langle \lambda_1 \rangle = 39.8 \pm 2.8$  and  $\langle \lambda_2 \rangle = 42.3 \pm 4.8 \mu\text{m}$ , respectively. Furthermore, the corresponding frequency of the flagellar beat for the cells closely match during the steady-swimming phase with an average of  $52 \pm 8$  and  $50 \pm 30$  rad s<sup>-1</sup>. The mean values of the wave variables for each cells in the three swimming phases are displayed in table.1.

Another important measure of the cells and the bundle is the linear (VSL) swimming velocity before and after the bundling. In the far field-to-locking phase, the velocities of the first and second cells are  $\langle VSL_1 \rangle = 35.2 \pm 4.6 \mu\text{ms}^{-1}$  and  $\langle VSL_2 \rangle = 12.2 \pm 3.5 \mu\text{ms}^{-1}$ , while the average swimming linear velocity of the bundle in the steady-swimming phase is  $42.15 \mu\text{ms}^{-1}$ . The increase in the swimming speed of the bundle is a direct consequence of adapt-

Table 1: Experimental results of time-dependant wave variables with a viscosity of 7 mPas.

Swimming Phases	$\langle {}^1K_0 \rangle$	$\langle {}^2K_0 \rangle$	$\langle {}^1A_0 \rangle$	$\langle {}^2A_0 \rangle$	$\langle \lambda_1 \rangle$	$\langle \lambda_2 \rangle$
Far Field	$7.3 \pm 0.8$	$8.9 \pm 1.09$	$12.5 \pm 0.7$	$9.4 \pm 0.8$	$40.1 \pm 2.6$	$36.01 \pm 0.8$
Spin-Rolling	$8.02 \pm 2.28$	$8.8 \pm 1.8$	$10.6 \pm 1.6$	$8.3 \pm 1.7$	$40.06 \pm 3.8$	$39.7 \pm 5.4$
Steady-Swimming	$7.9 \pm 1.1$	$8.2 \pm 0.9$	$7.5 \pm 1.3$	$6.1 \pm 1.5$	$39.8 \pm 2.8$	$42.3 \pm 4.8$

Table 2: Experimentally determined velocity and thrust force with a viscosity of 7 mPas.

Swimming Phases	$\langle VSL_1 \rangle$	$\langle VSL_2 \rangle$	$\langle VCL_1 \rangle$	$\langle VCL_2 \rangle$	$\langle \mathbf{f}_1 \rangle \times 10^{-11}$	$\langle \mathbf{f}_2 \rangle \times 10^{-11}$
Far Field	$35.2 \pm 4.6$	$12.2 \pm 3.5$	$56.3 \pm 24.0$	$40.1 \pm 15.2$	$1.2 \pm 0.0061$	$1.01 \pm 0.14$
Spin-Rolling	$36.06 \pm 7.3$	$32.1 \pm 9.6$	$59.0 \pm 25.8$	$50.3 \pm 25.7$	$1.12 \pm 0.24$	$0.95 \pm 0.313$
Steady-Swimming	$42.6 \pm 3.6$	$41.7 \pm 3.9$	$64.3 \pm 21.5$	$65.2 \pm 21.0$	$0.82 \pm 0.22$	$0.68 \pm 0.26$

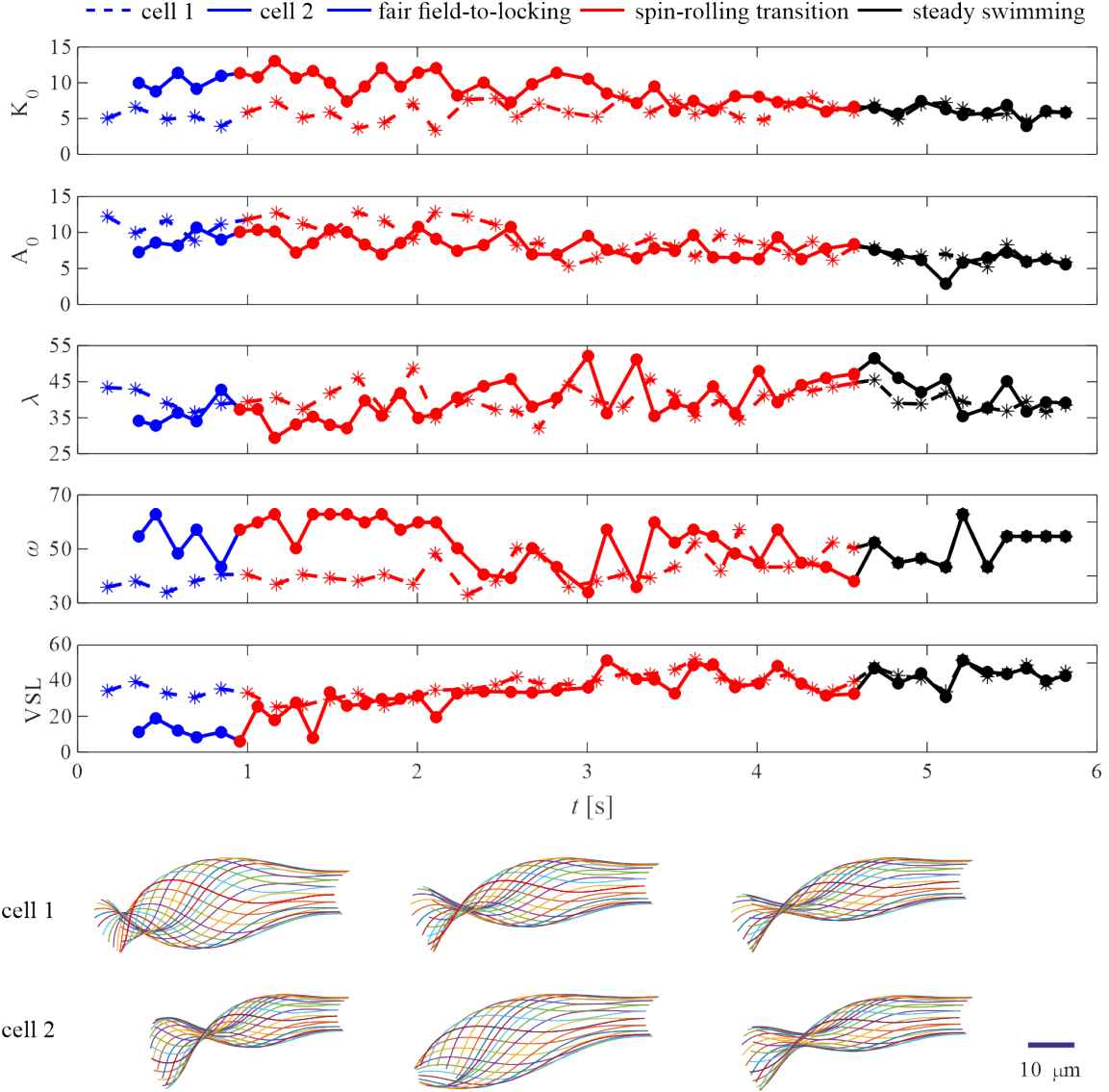


Fig. 4: Wave variables of two cells are measured during their transition from far field-to-locked phase to steady swimming phase in SP-TALP with a viscosity of 7 mPa s. From top to bottom: Mean flagellar curvature  $K_0$  in  $rad\ mm^{-1}$ ; amplitude rise  $A_0$  in  $rad\ mm^{-1}$ ; wavelength  $\lambda$  in  $\mu m$ ; beating frequency  $\omega$  in  $rad\ s^{-1}$ ; linear velocity VSL in  $\mu m\ s^{-1}$ ; reconstructed average flagellar shape for each swimming phase.

ing the flagellar waveform across the three phases. On average, an enhancement in the swimming speed is achieved as a consequence of bundling, and the swimming speed of the bundle is faster than that of the cells during any bundling phase. Furthermore it can be noted that the linearity ( $VSL/VCL$ ) in the trajectory of the bundle is greater than single cells'. Lastly, the thrust force produced by each cell decreases when they form the bundle, from an average thrust force in the far-field phase  $\langle \mathbf{f}_1 \rangle = (1.2 \pm 0.0061) \times 10^{-11} \mu N$  and  $\langle \mathbf{f}_2 \rangle = (1.01 \pm 0.14) \times 10^{-11} \mu N$  to  $\langle \mathbf{f}_1 \rangle = (0.82 \pm 0.22) \times 10^{-11} \mu N$  and  $\langle \mathbf{f}_2 \rangle = (0.68 \pm 0.26) \times 10^{-11} \mu N$  in the steady swimming phase resulting in a more efficient energy consumption. The results for the mean

linear and curvilinear velocities as well as the average thrust forces delivered by each cells are displayed in Table.2.

### 3.3 Transition in Low Viscosity Medium

In experiments with relatively low viscosity of  $\mu = 1.2\ mPa$ , the flagellar waveform of the three bundling phases are once again measured to determine the influence of each phase on the time-dependent wave variables. In this experiment, two cells on an parallel converging course (Fig.14) assemble into a bundle and undergo a 180 deg turn before entering the steady state swimming phase. In the far field-to-

locking phase, the averaged mean flagellar curvature of the first and second cells are  $\langle {}^1K_0 \rangle = 24.3 \pm 3.2$  and  $\langle {}^2K_0 \rangle = 31.01 \pm 5.2 \text{ rad mm}^{-1}$ , respectively. As the distance between the cells decreases, the mean flagellar curvature as well as the amplitude rise of the first and second cells remains almost uniform. The average amplitude rise are  $\langle {}^1A_0 \rangle = 5.9 \pm 0.1$  and  $\langle {}^2A_0 \rangle = 7.4 \pm 1.4 \text{ rad mm}^{-1}$ , respectively, as shown in Table.3. Finally, the wavelength of the first cell during this phase increases and decreases in a downward

fashion with an average of  $\langle \lambda_1 \rangle = 92.4 \pm 13.0 \mu\text{m}$ , while the average wavelength of the second cell increases linearly and its average is  $\langle \lambda_2 \rangle = 73.01 \pm 8.6 \mu\text{m}$ .

Once the heads of the two cells touch, they start the spin-rolling phase in which the two cells rotate about the common axis  ${}^i\mathbf{e}_1 \times {}^i\mathbf{e}_2$ . Note that the connection between the phases is continuous and the mean flagellar curvature of the first cell continues to remain

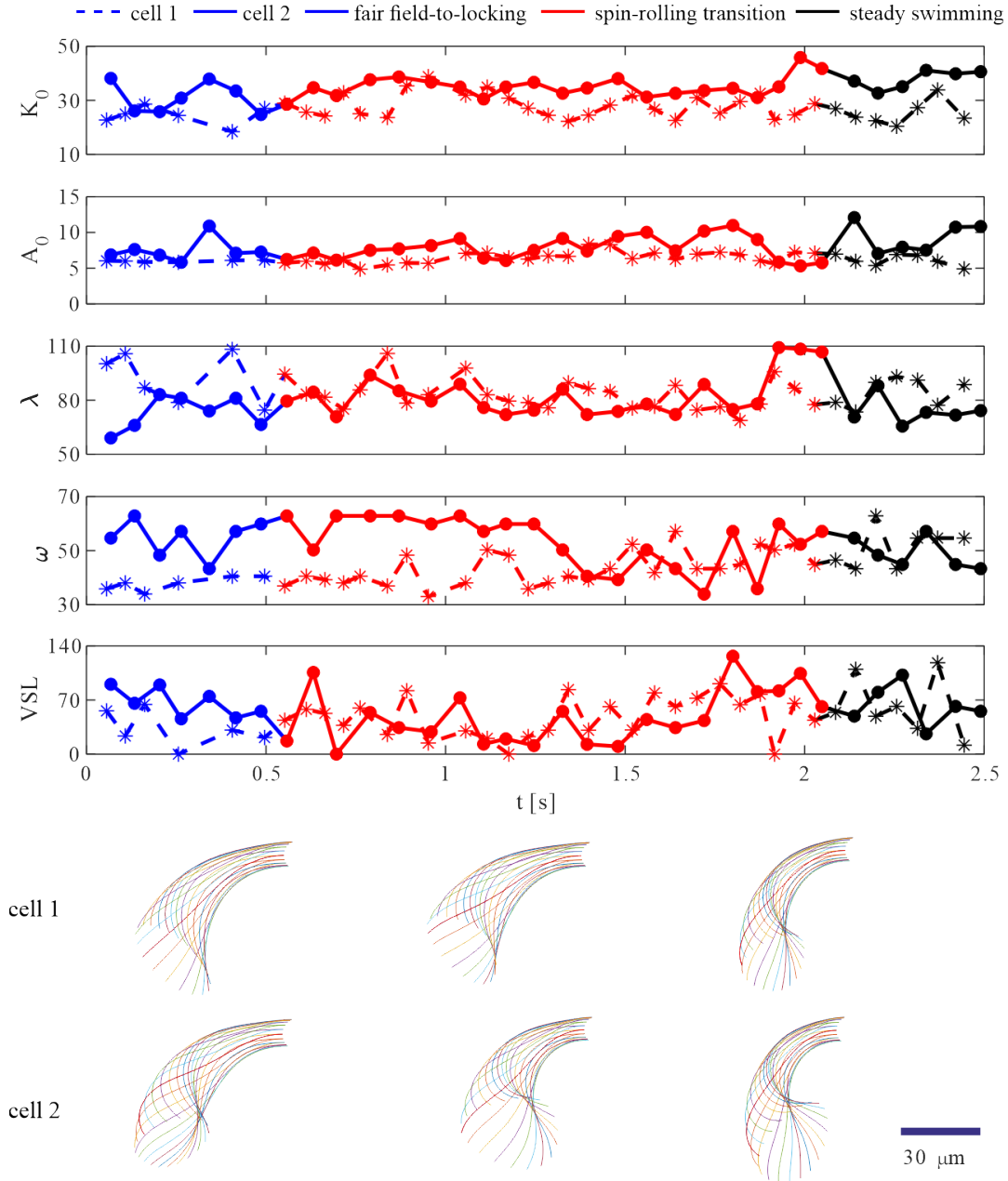


Fig. 5: Wave variables of two cells are measured during their transition from far field-to-locked phase to steady swimming phase in SP-TALP with a viscosity of 1.2 mPa s. From top to bottom: Mean flagellar curvature  $K_0$  in  $\text{rad mm}^{-1}$ ; amplitude rise  $A_0$  in  $\text{rad mm}^{-1}$ ; wavelength  $\lambda$  in  $\mu\text{m}$ ; beating frequency  $\omega$  in  $\text{rad s}^{-1}$ ; linear velocity VSL in  $\mu\text{m s}^{-1}$ ; reconstructed average flagellar shape for each swimming phase.

Table 3: Experimental results of time-dependant wave variables with a viscosity of 1.2 mPas.

Swimming Phases	$\langle {}^1K_0 \rangle$	$\langle {}^2K_0 \rangle$	$\langle {}^1A_0 \rangle$	$\langle {}^2A_0 \rangle$	$\langle \lambda_1 \rangle$	$\langle \lambda_2 \rangle$
Far Field	$24.3 \pm 3.2$	$31.01 \pm 5.2$	$5.9 \pm 0.1$	$7.4 \pm 1.4$	$92.4 \pm 13.0$	$73.01 \pm 8.6$
Spin-Rolling	$28.2 \pm 4.3$	$35.05 \pm 3.8$	$6.4 \pm 0.8$	$7.7 \pm 1.5$	$83.1 \pm 8.2$	$83.4 \pm 11.8$
Steady-Swimming	$25.4 \pm 4.08$	$37.7 \pm 3.07$	$6.1 \pm 0.7$	$9.3 \pm 1.9$	$84.6 \pm 7.2$	$73.9 \pm 6.8$

Table 4: Experimentally determined velocity and thrust force with a viscosity of 1.2 mPas.

Swimming Phases	$\langle VSL_1 \rangle$	$\langle VSL_2 \rangle$	$\langle VCL_1 \rangle$	$\langle VCL_2 \rangle$	$\langle \mathbf{f}_1 \rangle \times 10^{-12}$	$\langle \mathbf{f}_2 \rangle \times 10^{-12}$
Far Field	$32.8 \pm 21.6$	$67.0 \pm 17.3$	$178.1 \pm 105.7$	$186.4 \pm 87.6$	$1.2 \pm 0.38$	$0.41 \pm 0.96$
Spin-Rolling	$47.7 \pm 25.5$	$48.2 \pm 35.1$	$181.5 \pm 88.8$	$177.5 \pm 106.6$	$1.2 \pm 0.68$	$0.0709 \pm 0.65$
Steady-Swimming	$62.6 \pm 35.8$	$62.5 \pm 23.8$	$254.1 \pm 113.6$	$239.3 \pm 111.9$	$1.4 \pm 0.51$	$0.92 \pm 0.84$

constant, while that of the second cell remains almost constant in the first half of the spin-rolling phase and exhibit a slight increase in the second half. The average mean flagellar curvatures of the first and second cells during the spin-rolling phase are  $\langle {}^1K_0 \rangle = 28.2 \pm 4.3$  and  $\langle {}^2K_0 \rangle = 35.05 \pm 3.8$  rad mm<sup>-1</sup>, respectively. Note that the values presented here are kept positive in order to easily compare their magnitude but in this case the values of the flagellar curvature of both cells are opposite in sign which result in a repulsive force onto each other tail, producing the 180 deg turn. Similarly to the mean flagellar curvature, the amplitude rise of both cells remain constant throughout the phase. The average amplitude rise of the first and second cell during this phase are  $\langle {}^1A_0 \rangle = 6.4 \pm 0.8$  and  $\langle {}^2A_0 \rangle = 7.7 \pm 1.5$  rad mm<sup>-1</sup>, respectively. Finally, the wavelengths of both cells are similar and stay relatively constant throughout the spin rolling phase. The average are calculated as  $\langle \lambda_1 \rangle = 83.1 \pm 8.2$  and  $\langle \lambda_2 \rangle = 83.4 \pm 11.8$   $\mu m$ , respectively. Note that there is a noticeable match between the three variables throughout the spin-rolling phase.

Again, once the long axes of the two heads align after the 180 deg turn as shown in section C, the bundle starts the steady-swimming phase and we observe that the magnitude of the mean flagellar curvature and bending amplitude of the cells do not match. Furthermore, their flagellar wave are still out of phase and therefore do not validate the steady swimming phase. In this phase, the mean flagellar curvature of the first and second cells are  $\langle {}^1K_0 \rangle = 25.4 \pm 4.08$  and  $\langle {}^2K_0 \rangle = 37.7 \pm 3.07$  rad mm<sup>-1</sup>, respectively, while their corresponding bending amplitude are  $\langle {}^1A_0 \rangle = 6.1 \pm 0.7$  and  $\langle {}^2A_0 \rangle = 9.3 \pm 1.9$  rad mm<sup>-1</sup>, and no further noticeable change near the end of this phase

is observed. Similarly to the mean flagellar curvature and amplitude, there is a noticeable difference in the wavelength during the steady-swimming phase, and the first and second cells have  $\langle \lambda_1 \rangle = 84.6 \pm 7.2$  and  $\langle \lambda_2 \rangle = 73.9 \pm 6.8$   $\mu m$ , respectively. However, the corresponding frequency of the flagellar beat for the cells closely match starting from the end of the spin rolling phase to the steady-swimming phase with average of  $\approx 52$  and  $\approx 50$  rad s<sup>-1</sup>.

Finally the bundling gives a net increase in average linear velocity for the first cell. In the far field-to-locking phase, the velocities of the first and second cells are  $\langle VSL_1 \rangle = 32.8 \pm 21.6 \mu m s^{-1}$  and  $\langle VSL_2 \rangle = 67.0 \pm 17.3 \mu m s^{-1}$ , while the average swimming velocity of the bundle in the steady-swimming phase is  $\approx 62.5 \mu m s^{-1}$ . Moreover, swimming speed (VCL) increases by a net margin as shown in table.4.

#### 4 DISCUSSION

The time-dependent wave variables have been successfully extracted from two videoscopies that put on view the bundling process of two sperm cells in a high and low viscosity medium. The high viscosity video has shown to be much easier to analyze as the flagellar beat pattern of the cells shows a net dependence over the bundling process. This dependence is characterized by a synchronization of the wave variables as the heads of the cells align in the spin-rolling phase. As shown in Fig.4, the difference of magnitude between the respective wave variables of both cells gradually decrease throughout the transition and become equal in the steady swimming phase. The mean flagellar curvature and the bending amplitude become smaller while the wavelengths increase, leading to two relatively flat flagellar waves

with a small amplitude and a large wave propagation speed. Furthermore, the bundling process in this video demonstrates speed enhancement, agreeing with the former assumptions. An interesting displayed characteristic is the net difference in swimming speed between the two cells in the far field to locking phase which result in one cell (cell 1) boosting the swimming speed of the other cell (cell 2).

Unlike the high viscosity video, the low viscosity case exhibits a set of results that make drawing conclusions challenging. The flagellar shape of both cells are characterized by a large curvature and a small amplitude rise that stay constant along the swimming process. No synchronization happens after the spin rolling phase since the respective beat pattern of the cells stay out of phase. In the spin rolling phase, the cells undergo a 180 deg turn even though the cells are already aligned with each other as they meet on a parallel converging course, hence being already in a stable configuration in order to reach a synchronized swimming. This occurrence could be explained by 2 different reasons: First, the bundling causes the cells to change their course of action. In fact, cells swim on an average circular path and in this case the cells swim on circular paths that are opposite in direction. Hence the bundling has a direct effect on the 180 deg turn so that the cells can start swimming in one same circular path. The second reason could be related to a hydrodynamic interaction where the bundling has no cause over the spin rolling transition. Indeed, the respective wave variables happen to be equal in magnitude but opposite in sign which result in similar flagellar waves that are out of phase. This property induces repulsive forces to act on each other flagellum, hence making the cells rotate in opposite directions. The bundling phenomena hardly shows any influences on the wave variables, hence the low viscosity case requires to be analysed further in time to be able to compare it with the high viscosity case. However, an alignment in speed can be noted which is similar to the high viscosity case suggesting an eventual synchronisation.

Lastly, sperm bundling caught on camera is a rare occurrence leading to a lack of examples to draw from. A thorough study on the hydrodynamic interactions taking place between the bundled cells and the surrounding fluid could help enhance the understanding of the bundling phenomena and allowing a mathemat-

ical model to be created. Additionally, manual tracking over several thousand frames with relatively low resolution can lead to human errors and large times consumption. Automating the points placement could increase work efficiency in the future.

## 5 CONCLUSION

In this paper, high-speed videography and quantitative image analysis have been utilized to obtain time dependent wave variables that characterize the flagellar wave of sperm cells when those form a bundle close to a planar boundary surface. This work contributes to look, from a mathematical perspective, at the evolution of the flagellar wave of the sperm cells during transition from single to bundle in a relatively high and low viscosity fluid. In the high viscosity medium, sperm cells display synchronization of their flagellar curvature, bending amplitude and wavelength in order to increase their linear and curvilinear swimming velocity while reducing their respective force output. Further research must focus on finding the optimal wave variables magnitude from a bigger pool of bundling examples in order to successfully model a bundling of soft micro-robots that could efficiently swim in complex fluids actuated by weak magnetic fields. In the low viscosity medium, the results showed to be not obvious enough to draw any conclusions that could help drawing parallels with the high viscosity case. The lack of such is the consequence of too few data to work with. In this case, thorough studies of spatial variations within the dynamical system need to be undertaken in future works.

## 6 ACKNOWLEDGEMENTS

Here, I would like to thank I.S.M Khalil for his guiding and his patience. This work allowed me to get an outline of how a scientific research is conducted. Furthermore, I would like to thank Kaixuan Zhang for his great help to make the results as accurate as possible. I wish them the best of luck for their future works and discoveries to come in the field of soft micro robotic.

## REFERENCES

1. J. Hwang, Y. Jeong, J. Min Park, K. Hong Lee, J. HookHong, J. Choi, Biomimetics: forecasting the future of science, engineering, and medicine, In: *Internal Journal of Nanomedicine*, 5701-5713, (2015).

2. A.E. Hosoi and E. Lauga, Mechanical aspects of biological locomotion, In: *guest editorial*, 1259-1261, (2010).
3. E.M. Purcell, Life at low reynolds number, In: *AM. J. Phys.* 45, 3-11, (1977).
4. T. Qiu, T.C Lee, A.G. Mark, K.I. Morozov, R. Munster, O. Mierka, S. Turek, A.M. Leshansky, P. Fischer, Swimming by reciprocal motion at low reynolds number, In: *nature communications*, 5(1), (2014).
5. V. Magdanz, Y. Hamed, A. Klingner, M. Toubar, S. Misra, I.S.M. Khalil, Characterization of flagellar propulsion of soft microrobotic sperm in a viscous heterogeneous medium, In: *frontiers in Robotics and AI*, 6: 65, (2019).
6. V. Magdanz, J. Vivaldi, S. Mohanty, A. Klingner, M.I. Vendittelli, J. Simmchen, S. Misra, I.S.M. Khalil, Impact of segmented magnetization on the flagellar propulsion of sperm-templated microrobots, In: *Wiley-VCH GmbH*, 2004037, (2021).
7. A.V. Singh, M.H.D. Ansari, M. Mahajan, S.H. Srivastava, S. Kashyap, P. Dwivedi, V. Pandit, U. Katha, Sperm cell driven microrobots-emerging opportunities and challenges for biologically inspired robotic design, In: *micromachines*, 11(4):448, (2020).
8. J. Gray, G.J. Hancock, The propulsion of sea-urchin spermatozoa, In: *J.Exp. Biol.* 32, 802-814, (1955).
9. B.M. Friedrich, I.H. Riedel-Kruse, J. Howard, F. Jülicher, High-precision tracking of sperm swimming fine structure provides strong test of resistive force theory, In: *The Company of Biologists*, 1226-1234, (2010).
10. V. Magdanz, I.S.M. Khalil, J. Simmchen, G.P. Furtado, S. Mohanty, J. Gebauer, H. Xu, A. Klingner, A. Aziz, M.M Sanchez, O.G. Schmidt, S. Misra, Ironsperm: Sperm-templated soft magnetic microrobots, In: *SciencesAdvanced*, 6 (28) , (2020).
11. D.M. Woolley, Motility of spermatozoa at surfaces, In: *Reprod.* 259-270, (2003).
12. V. Magdanz, O.G. Schmidt, Spermbots: potential impact for drug delivery and assisted reproductive technologies, In: *EXPERT OPINION*, 1125-1129, (2014).
13. V. Magdanz, S. Sanchez, O.G. Schmidt, Development of a sperm-flagella driven micro-bio-robot, In: *Adv.Mater.* 6581-6588, (2013).
14. Y. Hamed, M. Tawakol, L. El Zahar, A. Klingner, S. Abdenadher, I.S.M. Khalil, Realization of a soft microrobot with multiple flexible flagella, In: *IEE International Conference on Biomedical Robotics and Biomechatronics*, 61-66, (2018).
15. H.S. Fisher, E.J. Palmer, J.M. Lassance, H.E. Hoekstra, The genetic basis and fitness consequences of sperm midpiece size in deer mice, In: *Nature Communications* 7,1-9, (2016).
16. T. Pizzari, K.R. Foster, Sperm Sociality: Cooperation, Altruism, and Spite, In: *PLoS Biol* 6(5), 925-931, (2008).
17. D.J.G. Pearce, L.A. Hoogerbrugge, K.A. Hook, H.S. Fisher, L. Giomi, Cellular geometry controls the efficiency of motile sperm aggregates, In: *J R Soc Interface*, (2018).
18. H.S. Fisher, L. Giomi, H.E. Hoekstra, L. Mahadevan, The dynamics of sperm cooperation in a competitive environment, In: *Proc. R. Soc B* 281: 20140296, (2014).
19. C.K. Tung, C. Lin, B. Harvey, A.G. Fiore, F. Ardon, M. Wu, S.S. Suarez, Fluid viscoelasticity promotes collective swimming of sperm, In: *SCIENTIFIC REPORTS*, 7:3152, (2017).
20. H. Moore, K. Dvorakova, N. Jenkins, W. Breed, Exceptional sperm cooperation in the wood mouse, In: *Nature* 418, 174-177, (2002).
21. W.E. Burnett, J. Heinze, Sperm bundles in the seminal vesicles of sexually mature *Lasius* ant males, In: *PLoS one*, 9(3), (2014).
22. K. Sasakawa, Sperm bundle and reproductive organs of carabid beetles tribe pterostichini (Coleoptera: Carabidae). In: *Naturwissenschaften* 94, 384-391, (2007).
23. I.S.M. Khalil, A. Klingner, S. Misra, Principles of propulsion by flagella ad cilia , In: *Mathematical Modelling of Swimming Soft Microrobots*, Chapter 5, 88-91, (2021).

## A VIDEOS

Two videocopies of bovine sperm cells where a bundling phenomena is taking place have been performed. The cells are trapped near a boundary surface in a high and low viscosity fluid of 7 mPas and 1.2 mPas respectively. Both videos have been realized with a camera scaled at  $1.15\text{pixel}/\mu\text{m}$ . The sequence can be observed in Fig.13 and Fig.14 for the high and low viscosity videos respectively, where each swimming phases are illustrated with 3 frames. The high viscosity video lasts 5.64s while the low viscosity is filmed within a time period of 3.91s. The path taken by the cells' heads in the high viscosity and low viscosity fluid are displayed in Fig.6 and Fig.7. In the high viscosity case, cell 1 undergoes 40 beat cycles while cell 2 performs 45 beat cycles. In the low viscosity case, cell 1 and cell 2 go through 39 and 34 beat cycles, respectively.

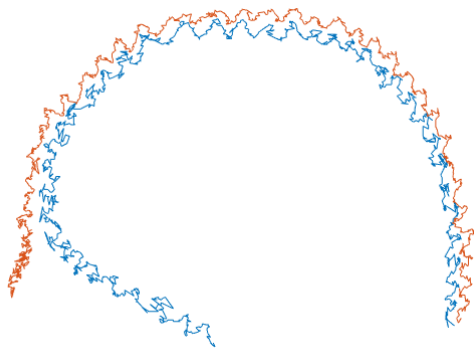


Fig. 6: Path taken by the sperm cells heads in the  $7mPas$  viscosity fluid (from left to right). The Blue curve represents cell 1 while the orange curve displays the path taken by cell 2.

In the high viscosity video, cell 1 is coming from the right and meets cell 2 from a 90 deg angle. Both cells form a bundle and go on swimming in a clockwise fashion following a circular average path.

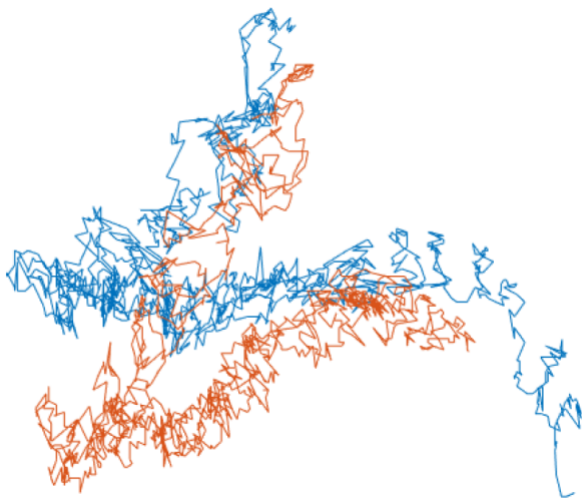


Fig. 7: Path taken by the sperm cells heads in the  $1.2mPas$  viscosity fluid (from right to left). The orange curve represents cell 1 while the blue curve displays the path taken by cell 2.

In the low viscosity video, cell 2 meets cell 1 from above on a parallel converging course. Both cells undergo a 180 deg turn before moving on as a bundle in the opposite direction from which they were coming.

## B MATLAB

Matlab is used to manually place 20 points along the centerline of the flagellum for each frame in order to extract the tangent angle with respect to the arc length and time. An snapshot of a frame with the manually placed points is shown in Fig.8.

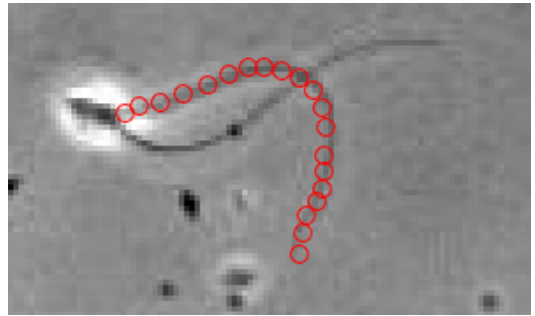


Fig. 8: Frame with points placed along the centerline of the flagellum of a cell.

As a result, the flagellar beat pattern for each cycle can be reconstructed using RFT matlab script which is based on Friedrich work [9]. Note that the beat pattern can be approximated as a sine wave and therefore the reconstructed flagellar wave must match a sine wave with the appropriate frequency as shown in Fig.9.

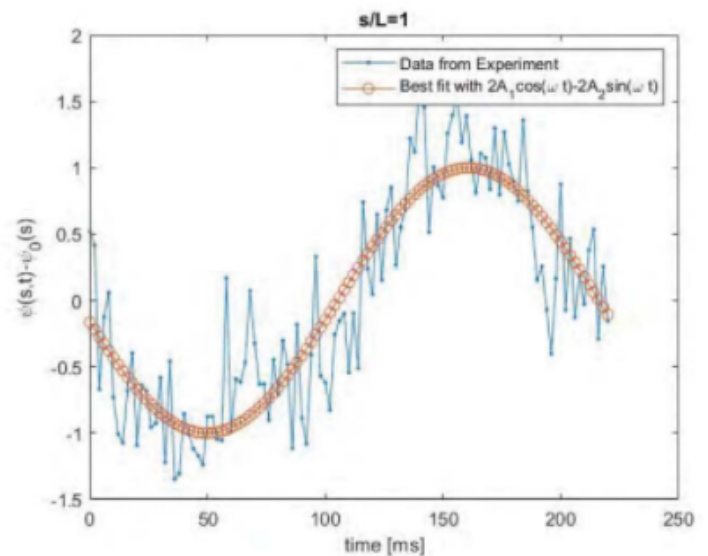


Fig. 9: Approximated beat pattern (blue) matched with a sine wave (red) with appropriate frequency.

If the matching holds true, the veracity of the wave variables can be taken for granted. Fig.10 shows the extraction of the wave variables for one beat cycle.

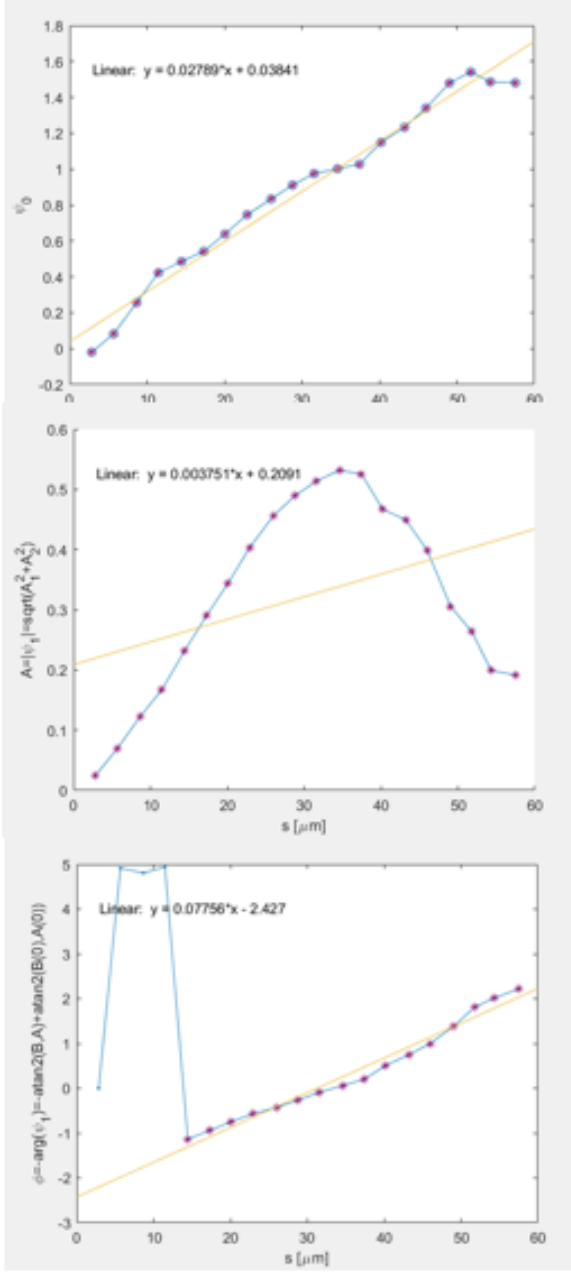


Fig. 10: Graphs to determine the wave-variables.

Fig.10 shows in this specific beat cycle that the curvature increases along the flagellum, the bending amplitude is at its maximum halfway through the flagellum length and the rate of wave propagation varies linearly along the length. It is worth mentioning that the accuracy of the points placements is not always optimal and can have several consequences on the Fourier modes as illustrated in Fig.11:

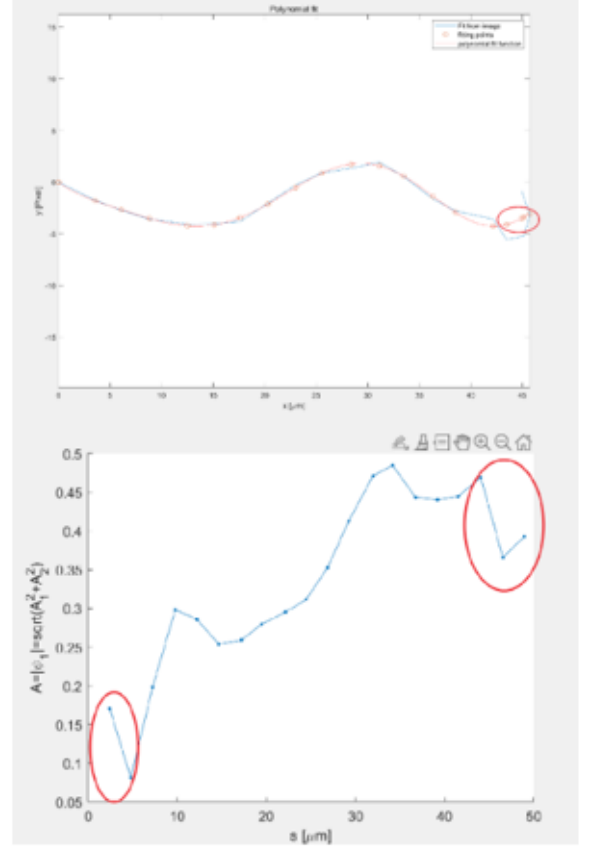


Fig. 11: Top: Discrepancies in the fitting curve of the polynomial fit marked by the red circle. Bottom: Distorted points within first fourier mode's absolute value marked here by the red circles.

These mismatches from the polynomial fit often located near the end of the flagellum result either from a lack of accuracy in the points placement or from an odd beating pattern. In that case, distorted points within the fourier modes functions must be left out when taking the fitting slopes so to prevent altering the wave variables' magnitude.

## C SPIN-ROLLING

### C.1 Rotational dynamics during Transition

During the spin-rolling transition phase, we assume that the heads rotate about the axis  $\mathbf{e}_1 \times \mathbf{e}_2$  and the relative rotational motion is resisted by a linear spring torque with elastic constant  $\kappa$ . Under these assumption, the moment on the first and second cells are:

$$\begin{aligned}
 {}^1\mathbf{M}(t) = & {}^1\mathbf{M}_{\text{head}}(t) + \kappa(\Theta_1(t) - \Theta_2(t)) \\
 & + \int_0^{L_1} \mathbf{r}_1(s, t) \times \mathbf{f}_1(s, t) ds = 0, \quad (10)
 \end{aligned}$$

$$\begin{aligned}
{}^2\mathbf{M}(t) = & {}^2\mathbf{M}_{\text{head}}(t) - \kappa(\Theta_1(t) - \Theta_2(t)) \\
& + \int_0^{L_2} \mathbf{r}_2(s, t) \times \mathbf{f}_2(s, t) ds = 0,
\end{aligned} \tag{11}$$

where  ${}^1\mathbf{M}_{\text{head}}(t)$  and  ${}^2\mathbf{M}_{\text{head}}(t)$  are the hydrodynamic torque on the head of the first and second cell, respectively. Note that the hydrodynamic torque on the head is linearly proportional to the angular velocity as  ${}^i\mathbf{M}_{\text{head}}(t) = 8\pi\mu ab^2 C_2 \Omega_i(t)$ . Given the identical geometry of the sperm heads, here we define  $C = {}^1 C_2 = {}^2 C_2$ . Combining the above expressions, we have:

$$\begin{aligned}
8\pi\mu ab^2 C (\Omega_1 - \Omega_2) + 2\kappa (\Theta_1 - \Theta_2) \\
+ {}^1\mathbf{M}_{\text{flag}} - {}^2\mathbf{M}_{\text{flag}} = 0,
\end{aligned} \tag{12}$$

The solution of Equation (12) satisfies

$$\begin{aligned}
\Delta\Theta(t) = & \left( \Delta\Theta_0 - \frac{1}{8\pi\mu ab^2 C} \int_0^t ({}^1\mathbf{M}_{\text{flag}} \right. \\
& \left. - {}^2\mathbf{M}_{\text{flag}} \exp\left(-\frac{\kappa}{4\pi\mu ab^2 C} t\right) dt \right) \\
& \exp\left(-\frac{\kappa}{4\pi\mu ab^2 C} t\right),
\end{aligned} \tag{13}$$

where  $\Delta\Theta = \Theta_1 - \Theta_2$  is the difference in angular position between the heads and  $\Delta\Theta_0$  is the initial difference in  $\Delta\Theta$  when the heads contact. Further,  ${}^i\mathbf{M}_{\text{flag}}$  is the moment of the  $i$ th flagella and can be calculated using the third term in Equations (8) and (9). Therefore, the characteristic time of the solution (13) is,  $\tau = 4\pi\mu ab^2 C / \kappa$ , and there is a direct and inverse relation with the viscosity of the medium and the elastic constant between the heads. Note that the difference in angular position  $\Delta\Theta(t)$  consists of two components, an exponential decay function,  $\exp(-\kappa/(4\pi\mu ab^2 C)t)$ , and a sinusoidal function,  ${}^1\mathbf{M}_{\text{flag}} - {}^2\mathbf{M}_{\text{flag}}$ . The exponential decay function is a result of the energy loss in low- $Re$  flow and the spring adhesion, whereas the sinusoidal function is a result of the energy transfer between the distributed contractile and the elastic elements of the active flagellum.

Fig. 12 shows the time response of  $\Delta\Theta(t)$  for two representative viscosities of 1.2 and 7 mPa s and different initial conditions. For  $\Delta\Theta = \pm 90^\circ$ , the two heads

align at a faster rate at  $\mu = 1.2$  mPa s for the same elastic constant, as shown in Fig. 12(a). Similarly, for  $\Delta\Theta = \pm 180^\circ$ , the two heads align at characteristic times of 370 and 1500 ms at viscosities of  $\mu = 1.2$  and  $\mu = 7$  mPa s, respectively, as shown in Fig. 12(b).

Note that propagating waves are mostly in unsynchronization during the spin-rolling transition phase and a non-zero phase shift is likely to be present between  ${}^1\mathbf{M}_{\text{flag}}$  and  ${}^2\mathbf{M}_{\text{flag}}$ . Therefore, the time response of  $\Delta\Theta(t)$  is calculated for phase angles  $\phi$ , as shown in Fig. 12(c), which show that for all values of  $\phi$ , the time response of  $\Delta\Theta$  will be oscillatory with an exponentially decreasing amplitude.

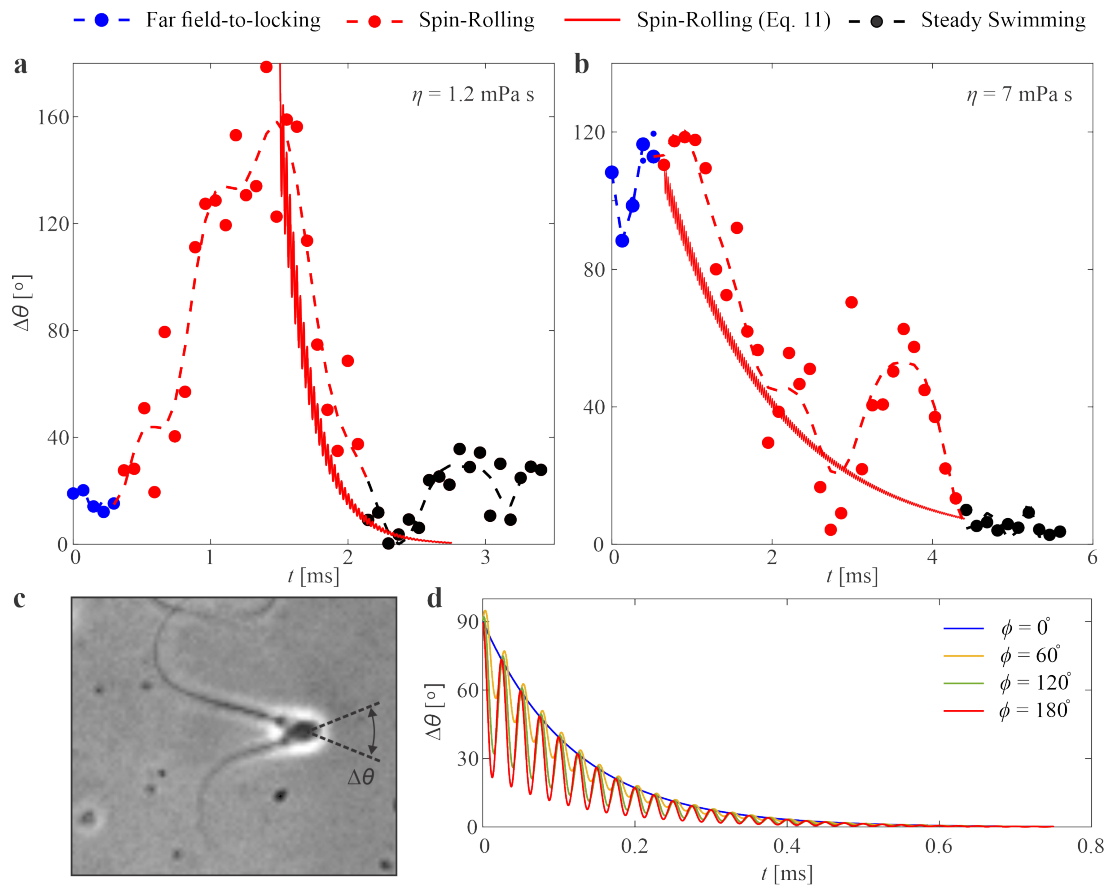


Fig. 12: The angle,  $\Delta\Theta(t)$ , between the axes  ${}^1\mathbf{e}_1$  and  ${}^2\mathbf{e}_1$  decreases exponentially to zero regardless of the initial angle and viscosity  $\mu$ . (a) At  $\mu = 1.2$  mPa s, measured convergence time from  $\Delta\Theta = \pm 180^\circ$  is less than 1 s. (b) At  $\mu = 7$  mPa s, measured convergence time from  $\Delta\Theta = \pm 90^\circ$  is 3.5 s. (d) The (c)  $\Delta\Theta(t)$  is measured during the three phases for  $\mu = 7$  mPa s. (c)  $\Delta\Theta$  oscillates with an exponentially decreasing amplitude for all values of the phase angles,  $\phi$ . (d) During spin-rolling,  $\Delta\Theta$  converges exponentially to zero.

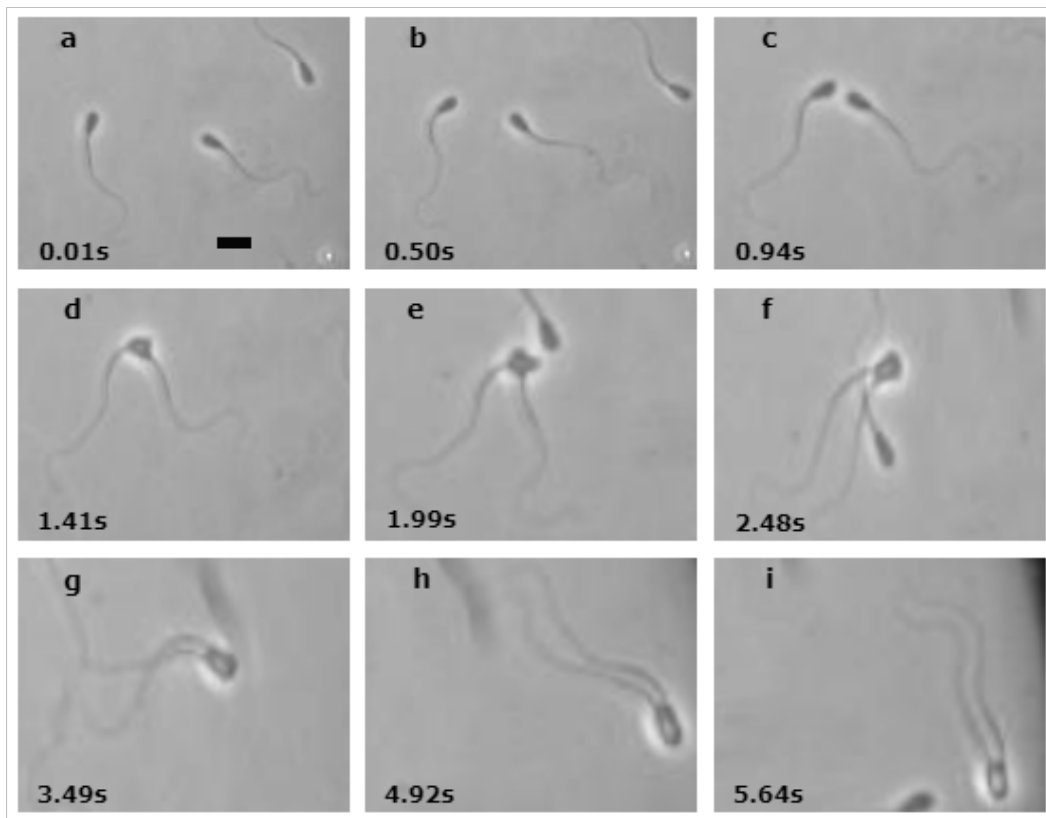


Fig. 13: Two sperm cells assemble into a sperm bundle in SP-TALP with a viscosity of 7 mPa s. (a-c) In the far field-to-locking phase, each cell is influenced by the flow field created by neighbor swimming cells. (d-f) In the spin-rolling transition phase, the angle between  ${}^1\mathbf{e}_1$  and  ${}^2\mathbf{e}_2$  is adjusted and the cells are in equilibrium. (g-i) In the steady-swimming phase, the 2 flagella adjust themselves to undulate in phase. Scale bar is  $10\mu\text{m}$ .

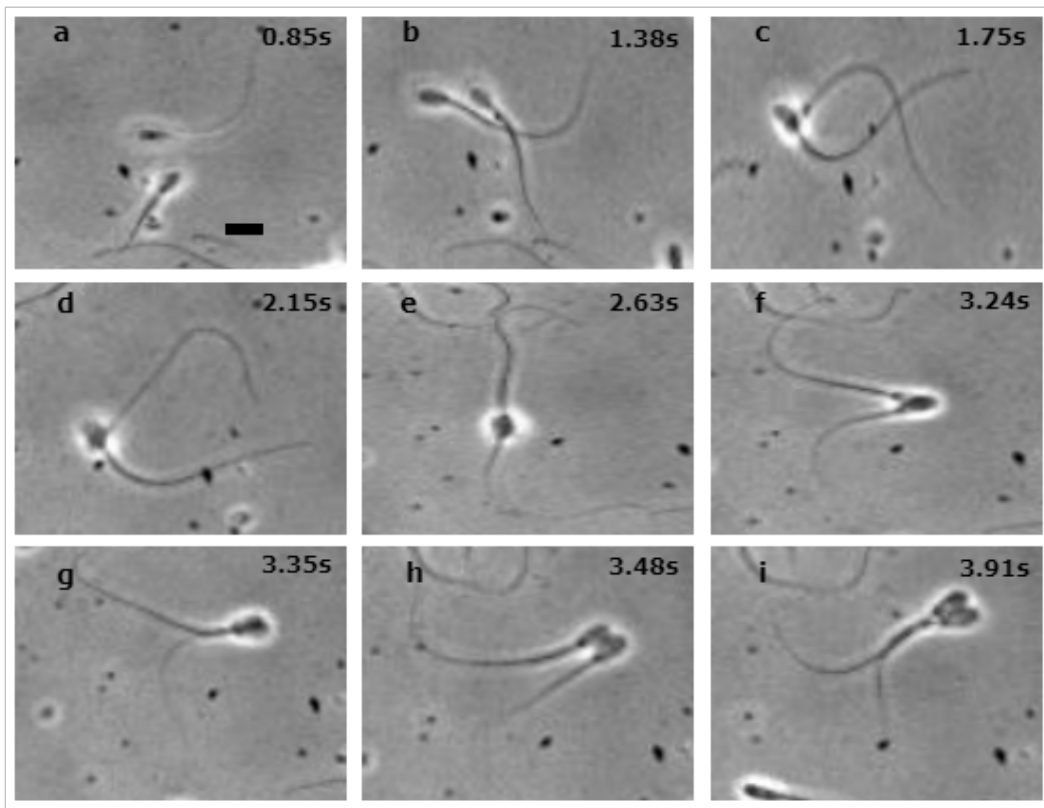


Fig. 14: Two sperm cells assemble into a sperm bundle in SP-TALP with a viscosity of 1.2 mPas. (a-c) In the far field-to-locking phase, each cell is influenced by the flow field created by neighbor swimming cells. (d-f) In the spin-rolling transition phase, the angle between  ${}^1\mathbf{e}_1$  and  ${}^2\mathbf{e}_2$  undergoes a 180 degrees turn. In the steady-swimming phase, the beat patterns remain out of phase. Scale bar is  $10\mu\text{m}$ .